RESEARCH ARTICLE

ADVANCED OPTICAL MATERIALS
www.advopticalmat.de

Spectroscopic Ellipsometry Characterization and Radiative Limit Modeling of Bismuth-Based Perovskite-Inspired Absorbers for Indoor Photovoltaics

Aleksi Kamppinen, G. Krishnamurthy Grandhi, Mahboubeh Hadadian, Sami Toikkonen, Sirius Yli-Paavola, Paola Vivo,* and Kati Miettunen**

Lead-free bismuth-based perovskite-inspired materials (Bi-PIMs) are emerging as wide bandgap semiconductors for sustainable optoelectronic applications, including indoor photovoltaics (IPVs). Computational modeling is a powerful tool to understand and optimize their device performance. However, device-relevant thin film optical constants for these absorbers remain scarce, limiting quantitative optical and electrical design. Here, for the first time the optical constants of two promising thin-film Bi-PIMs—Cu_2AgBiI_6 and $Cs_3Bi_2I_6Br_3$—are determined using spectroscopic ellipsometry. The applied graded effective medium approximation model is supported by the atomic force microscopy and scanning electron microscopy characterizations of varying film thicknesses. A realistic planar device stack is then simulated under both AM1.5G solar and 1000 lx indoor spectra. Under indoor conditions (1000 lx, 4000 K color temperature), the optical photocurrent limits are ca. 91 µA cm^{-2} for Cu_2AgBiI_6 and ca. 32 µA cm^{-2} for $Cs_3Bi_2I_6Br_3$ with the corresponding radiative-limit efficiencies of ca. 42 % and ca. 18 %, respectively. These results reveal a significant optical margin and motivate efforts to suppress nonradiative recombination and improve charge transport. More broadly, the extracted optical constants enable accurate photogeneration estimation for optoelectronic device modeling, providing insights into current performance limitations of Bi-PIM devices and guiding strategies to overcome them.

1. Introduction

Indoor photovoltaics (IPVs) are an emerging trend in the field of photovoltaics.[1–4] The concept involves harvesting ambient light to power devices around us 'on the spot', where they are used, thereby improving energy efficiency in built environments and reducing the need for intermediate steps, such as electricity transmission and storage. Wide-bandgap (E_g) absorbers are particularly suitable for indoor light harvesting, in contrast to the lower bandgap materials optimized for outdoor solar applications[5]. Detailed balance analyses predict single junction limiting efficiencies of ≈50 % for band-gaps in the range of 1.7–2.0 eV under representative indoor spectra, significantly higher than the outdoor theoretical limit at any E_g.[1] Currently, the IPV market is dominated by amorphous silicon.[2,3] However, promising results have recently been reported for organic photovoltaics,[6] dye-sensitized solar cells,[7] and perovskite solar cells.[1,8] Among these emerging IPV technologies, perovskite solar cells have demonstrated record IPV efficiencies (>40 %)[8] due to their high defect tolerance and facile bandgap tunability. However, the lead toxicity associate with perovskites underscores the urgent need for sustainable, lead-free alternatives.[9]

Lead-free, bismuth-based perovskite inspired materials (Bi-PIMs) offer a compelling route to achieve the desired wide-band-gaps with high compositional stability and a benign toxicology profile.[10–12] Among these, Cu_2AgBiI_6 (CABI) and $Cs_3Bi_2I_6Br_3$ (CBI) feature optical bandgaps of ca. 2.0 eV and ca. 2.4 eV, respectively—placing CABI near the optimal range for IPVs, while CBI serves as a useful high E_g reference. CABI is a unique PIM composition for its inherently low exciton binding energy (25 meV) and high defect tolerance, making it an ideal candidate for wide-bandgap (≈ 2.0 eV) IPV applications.

Although promising initial indoor device power conversion efficiencies (PCEs) of 5–6 % (1000 lx illuminance) have been demonstrated for CABI,[13] further progress is hindered by the lack of insights from optoelectronic simulations enabled by

A. Kamppinen, M. Hadadian, S. Yli-Paavola, K. Miettunen
Department of Mechanical and Materials Engineering
University of Turku
Vesilinnantie 5, Turku 20500, Finland
E-mail: aleksi.kamppinen@utu.fi; kati.miettunen@utu.fi

G. K. Grandhi, S. Toikkonen, P. Vivo
Hybrid Solar Cells
Faculty of Engineering and Natural Sciences
Tampere University
P.O. Box 541, Tampere FI-33014, Finland
E-mail: paola.vivo@tuni.fi

The ORCID identification number(s) for the author(s) of this article can be found under https://doi.org/10.1002/adom.202503237

DOI: 10.1002/adom.202503237

device-relevant optical constants ($n(\lambda)$, $k(\lambda)$) measured on the thin films typically used in IPV architectures. To date, only a few studies have employed spectroscopic ellipsometry (SE) to extract optical constants for Bi-based PIMs. For example, Valastro et al. investigated Bi-based $A_3Bi_2X_9$-type single crystals by ellipsometry providing insights especially on the excitonic and continuous bands, exciton binding energies, and their temperature dependence based on the Critical Point analysis of ellipsometry data.[14] However, thin film n and k data for CABI suitable for quantitative optical/optoelectronic modeling remain scarce.

Therefore, it is imperative to determine the optical constants—the complex index of refraction (n and k)—for CABI using spectroscopic ellipsometry to fill this current gap in the literature. The complex index of refraction of a material defines its interaction with light: the real part (n) typically governs refraction, while the imaginary part (k) describes absorption. Accurate knowledge of these optical constants enables precise modelling of reflection, transmission, local absorption, and photogeneration (G_{ph}) in a device across wavelengths. Therefore, complex refractive index spectra are critical for optical and optoelectronic modeling for optimizing device performance in a wide range of optoelectronic applications. For example, considering photovoltaic performance, the complex refractive index defines the reflectance at the material interfaces according to the Fresnel laws and the absorption in the absorber. Because n is typically larger than k (in non-metallic materials), n is especially important for determining and, ideally, minimizing the reflectance of a solar cell. k on the other hand is interconvertable with the absorption coefficient (α) making it an important parameter for maximizing the absorption. Spectroscopic ellipsometry is a powerful, yet underutilized technique for determining the optical properties of PV materials.[15]

In this study, we determine $n(\lambda)$ and $k(\lambda)$ for thin film CABI and CBI via spectroscopic ellipsometry for the first time, supported by atomic force microscopy (AFM) and scanning electron microscopy (SEM) to validate the optical model applying graded Bruggeman effective medium approximation (EMA) layer for the studied films. We apply the obtained optical constants data to estimate the previously uncertain practical maximum achievable photogeneration limits and radiative recombination-limited PCEs of CABI and CBI devices under the white light-emitting diode (WLED) indoor spectra of different color temperatures (2700 to 6500 K) and the reference AM1.5G solar irradiance. The obtained optical photocurrent density (J_{ph}) limit of ca. 91 μA cm^{-2} for CABI under 3 W m^{-2} indoor illumination translates into a radiative limit PCE of ca. 42 % with the simulated device stack. Finally, we investigate the effect of absorber layer thickness on the device performance, providing insights for device design. The results quantify the optical margin available for these emerging Bi-PIM IPVs, identify charge collection and nonradiative losses as the dominant remaining bottlenecks, and provide the necessary optical inputs for electrical modeling and optical design. Therefore, we advance the development of Pb-free Bi-PIMs for efficient power conversion of indoor illumination and enable further research on these promising IPVs.

2. Results and Discussion

2.1. Film Thickness, Coverage, and Roughness Evaluation

Ellipsometry is sensitive to both film thickness and surface roughness. Therefore, we applied SEM and AFM to better understand the sample structure, specifically the thickness and morphology of the films (Figures S1–S5, Supporting Information). SEM images (Figures S1 and S2, Supporting Information) indicated good overall sample coverage, although some regions of exposed substrate remained still visible. To account for this, AFM was used to extract actual height distributions (Figure S4, Supporting Information) in addition to describing the peaks and valleys of the sample surfaces. In this analysis, the substrate surface served as the height reference point.

AFM height distributions showed that both CABI and CBI thicknesses increased with precursor concentrations as intended (Figure S4, Supporting Information). The most frequent height values were ca. 56 , 112 , and 272 nm for the CABI samples and ca. 52 , 70 , and 162 nm for the CBI samples of varied precursor concentrations. Additional peaks at lower heights could be observed, especially in CBI samples (Figure S4, Supporting Information). Otherwise, the height distributions resembled normal distributions. The origin of the small peaks at low heights is somewhat uncertain. The peaks could originate from isolated small grains or a very thin, nearly continuous film. On the other hand, they could represent the substrate surface.

From SEM and AFM analysis, we conclude that the samples were rough and the void volume fraction f (material volume fraction $1-f$) increased (decreased) quasi-continuously from the substrate surface to the maximum sample height. Thus, we applied graded EMA layer in the ellipsometry analysis to model the sample films on top of the silicon substrate (**Figure 1a**). To fit the sample structure, that is, film thickness (t) and void volume fraction (f) distribution, and initial optical constants (n and k), a general oscillator model with three Tauc-Lorentz oscillators was first applied (Figure 1b; Tables S1–S4, Supporting Information).

The chosen optical model was fitted to the ellipsometry data for each sample individually and the fitted sample structures were compared to the AFM data (**Figure 2**). The thicknesses corresponding to 50:50 volume ratio between the sample and void (f_{50}) obtained from SE and AFM, respectively, agreed well, as shown in Figure 2. The void volume fractions obtained from SE by fitting slightly underestimated the variance of height distributions, as evident from the sharper fitted distributions compared to the AFM results (Figure S5, Supporting Information). Altogether, the applied graded EMA model, with the fitted sample specific t and f, was found to model the rough samples reasonably well and the structure parameters were fixed for more accurate optical constant extraction.

Considering the possibility of the small peaks at low heights (Figure S4, Supporting Information) actually representing the substrate surface, the zero level should be fixed slightly differently in that case. This alternative AFM zero-point determination was tested and it produced slightly different height distributions but basically equal agreement between the ellipsometry and AFM data was obtained (Figure S6, Supporting Information). The change would not affect the ellipsometry analysis in any case

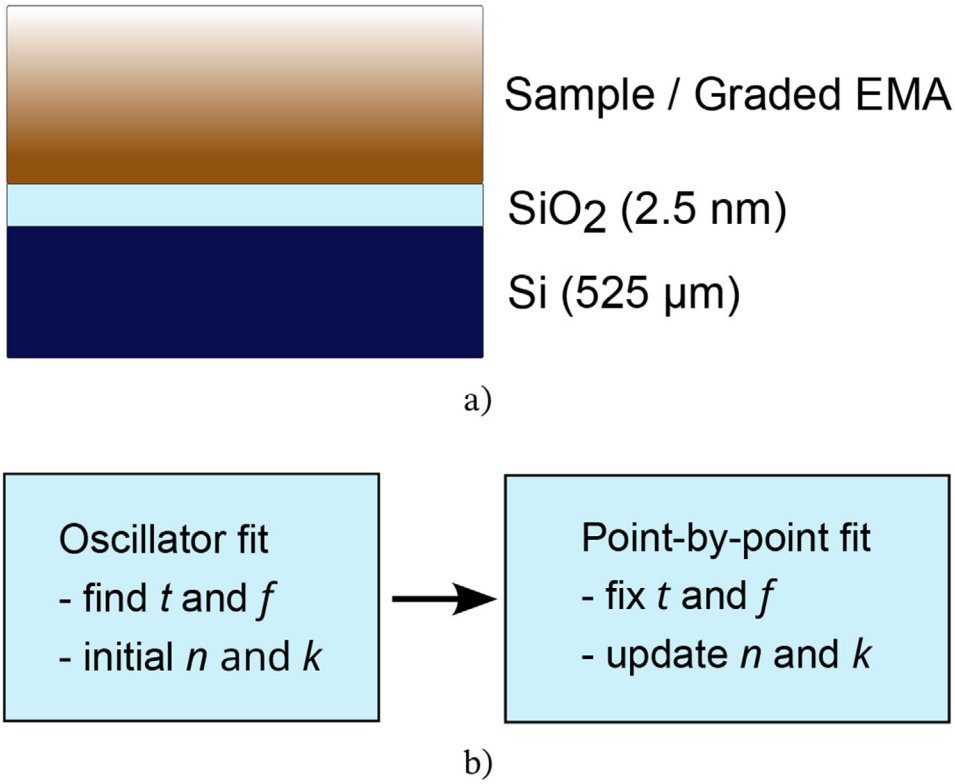

Figure 1. Ellipsometry model and analysis. a) Optical stack used in SE: Si | SiO_2 | sample film: graded EMA roughness (21 sublayers) | air. Figure is not to scale. b) Analysis workflow.

because the ellipsometry model and the structure parameters t and f were fixed based on the fitting to the ellipsometry data. AFM was conducted to be sure that the fitted sample structure was realistic.

In general, smooth films are preferred for ellipsometry. Therefore, the sample roughness, that remains with certain materials and/or preparation methods, required careful consideration to ensure accurate ellipsometry analysis. One potential issue arising from roughness is scattering because it might cause depolarization, which would require more complex Stokes vector-Mueller matrix calculus.[16] Despite the rough samples, depolarization was measured to be small (Figure S7, Supporting Information) meaning that the polarization state of the detected light was well defined to a large degree here. Therefore, Mueller matrix effects were negligible (because of the small depolarization). Another point to consider was the proper modeling of the roughness.[17] We applied quasi-continuous graded EMA layer with twenty-one sublayers to model the samples to consider the roughness and the film structure agreed well with the AFM results as presented above. The graded EMA model has also been successfully applied for rough samples in the literature.[18]

2.2. Optical Characterization

With the structure fixed, we applied point-by-point fitting to find the optical constants n and k for each sample individually. The fits reproduced the experimental ellipsometer data (the amplitude ratio Ψ and the phase difference Δ) well especially in the case of the thinner samples, as shown in **Figure 3** and Figures S8 and S9 (Supporting Information). The fits for the thickest films deviated from the measurements in places while capturing the main features (Figures S8 and S9, Supporting Information). The mean square error (MSE) increased as the sample thickness increased (Figure S10, Supporting Information). A point-by-point arithmetic mean over the individually fitted spectra among the acceptable MSE samples ($CABI_{50nm*}$, $CABI_{50nm}$, $CABI_{77nm}$, and $CABI_{78nm}$ and CBI_{40nm}, CBI_{45nm}, and CBI_{59nm}, respectively) was applied to obtain our result for the optical constants.

The obtained optical constants of CABI and CBI are presented as the complex index of refraction (n, k) and the complex dielectric constant (ε_1, ε_2), see **Figure 4**. These two equivalent representations should be interconvertible. Due to the averaging of optical constants over several samples, the presented (n, k) and (ε_1, ε_2) are not strictly interconvertible, but they are very close (Figure S12, Supporting Information). They are both shown here because both representations are frequently applied to represent the optical properties of materials.

n(CABI) increased from ca. 1.9 at 300 nm to ca. 2.6 at 435 nm and almost to 3.0 at 610 nm before a slight decline and the smooth area of ca. 2.5 from 1200 nm onwards (Figure 4a; Figure S11, Supporting Information). k(CABI) showed a broad absorption onset at around 610 nm and another peak at ca. 425 nm. k(CABI) was ca. 0.8 at the first shoulder (at 565 nm) corresponding to a high absorption coefficient (ca. 1.7×10^5 cm^{-1}), which agrees with the literature.[19–21] Equivalently, ε_1(CABI)

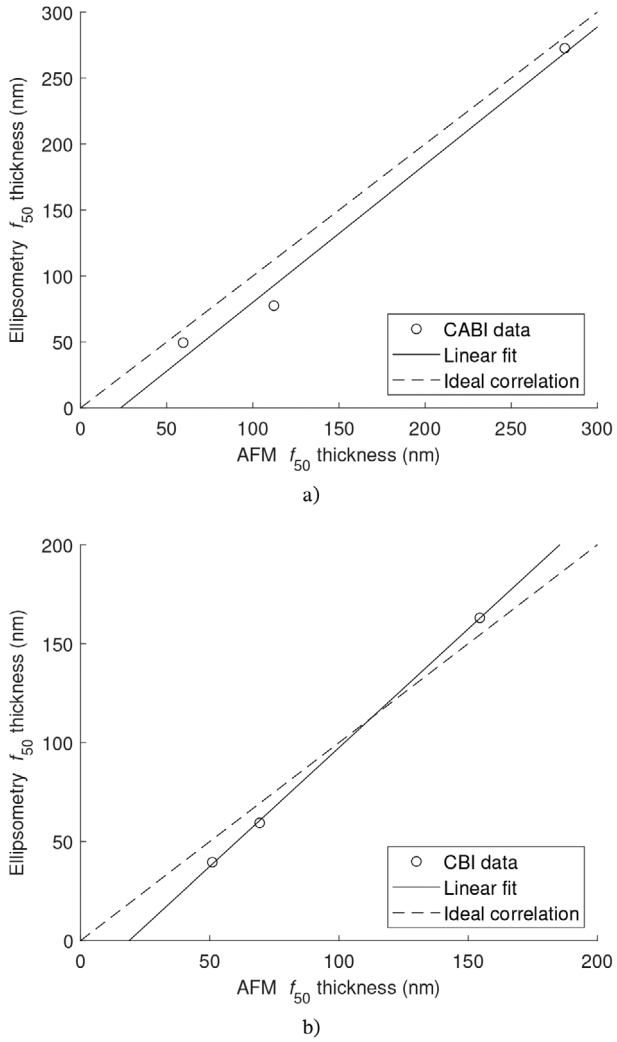

Figure 2. Agreement between AFM and ellipsometry thickness metrics. a) CABI and b) CBI: f50 thickness from SE versus AFM derived median height for films prepared from varying precursor concentrations on silicon substrates.

increased from ca. 6.5 at 1 eV to ca. 8.8 at 2 eV before decreasing to ca. 6.7 at 2.3 eV, ca. 6.0 at 2.85 eV and yet again to ca. 2.7 at 4 eV (Figures 4c; Figure S11, Supporting Information). ε_2(CABI) increased from ca. 0.4 at 1 eV to ca. 4.3 at 2.2 eV, showed another peak of 5.3 at 2.9 eV, and decreased from 5 to ca. 4.5 between 3 and 4 eV.

n(CBI) was slightly larger than *n*(CABI) throughout the studied range. *n*(CBI) increased from ca. 2.1 at 300 nm to ca. 2.9 at 390 nm (the first peak) and to ca. 3.4 at 525 nm (the second peak) before a smooth decline to ca. 2.6 at 1000 nm (Figures 4b; Figure S11, Supporting Information). *k*(CBI) also showed a broad but slightly sharper absorption onset at around 530 nm compared with *k*(CABI). We observed two peaks in *k*(CBI) spectrum: the first of ca. 0.9 at 500 nm and the second of ca. 1.5 at 340 nm. Correspondingly, ε_1(CBI) increased from ca. 6.9 at 1 eV to ca. 11.2 at 2.35 eV (the first peak) and decreased to ca. 2.7 at 4 eV showing another peak of ca. 7.7 at 3.1 eV in between (Figures 4d; Figure S11, Supporting Information). ε_2(CBI) showed one peak of ca. 5.5 at 2.45 eV and another wider peak of ca. 7.5 at 3.5 eV. A slightly higher absorption coefficient at the first peak ($\approx 2.2 \times 10^5$ cm^{-1}) was obtained here compared with a reported value for single crystal $Cs_3Bi_2I_9$ in the literature.[14]

The extracted sample specific optical constants varied moderately, that is, relative changes were ca. 10 % for CABI and ca. 30 % for CBI right above the bandgap (Figure S13, Supporting Information). The optical constants from the thinnest samples were concluded to give the most reliable result for the *n* and *k*, consistent with the literature.[22] Even larger relative changes have been detected for the optical constants of more common perovskites like MAPbI3 between different studies which was observed to probably originate from the surface roughness.[22] In addition to the different thickness samples, we paid attention to the roughness modeling as discussed above. In the future, smoother films and comparison to the first principles calculations could potentially help to reduce the sample-to-sample variation and deepen the understanding of underlying optical transitions.[23] However, preparing smoother films may not be straightforward in practice.

We further studied the sensitivity of the determined optical constants to the model properties, that is, the number of graded EMA sublayers and the roughness characterized by the rate of change of the void volume fraction (*f*) in the graded EMA layer (Figure S5, Supporting Information). Different number of sublayers (11, 21, and 31) had an insignificant effect on the fitted layer thickness (Figure S14, Supporting Information). However, the fitted roughness was consistent only for 21 and 31 sublayers, while the roughness was different for some samples with 11 sublayers. 21 sublayers was concluded necessary and sufficient number of sublayers. The effect of the number of graded EMA sublayers on *n* and *k* was mostly small and it was related to the roughness (Figures S15 and S16, Supporting Information). Therefore, the effect of the roughness was further studied. The increased roughness was observed to slightly increase *n*, but the effect on *k* varied between the different samples: *k* decreased for most of the individual samples, but it decreased for some (Figures S17 and S18, Supporting Information). Altogether, the effect was within the same order of magnitude as the sample-to-sample variance. MSE was noted to maintain at a similar level or slightly increase for the artificially added roughness (Figure S19, Supporting Information).

We compared different methods previously applied for similar materials, namely Tauc plot,[21,24–27] Elliott's model,[14,19,28] and Critical Point fitting,[14] to determine the band-gaps of CABI and CBI, respectively, based on the optical constant data (**Table 1** and Figures S5 and S6 and S20–S22, Supporting Information). Tauc plot produced the smallest band-gaps for both materials: 1.98 eV for CABI and 2.33 eV for CBI. The values by Elliott's model and Critical Point fitting agreed well to one another despite small differences and they were 0.05–0.1 eV larger compared with those of Tauc plot for both materials, respectively. Tauc plot has previously demonstrated a direct gap of 1.95 eV[21] while Elliott's model fit has produced slightly larger values of 2.06 eV[19] and larger (increasing with the decreasing temperature)[28] for CABI. We obtained similar values including the difference between the methods which highlights that the excitonic nature of these materials makes the extracted band-gap values method-dependent.

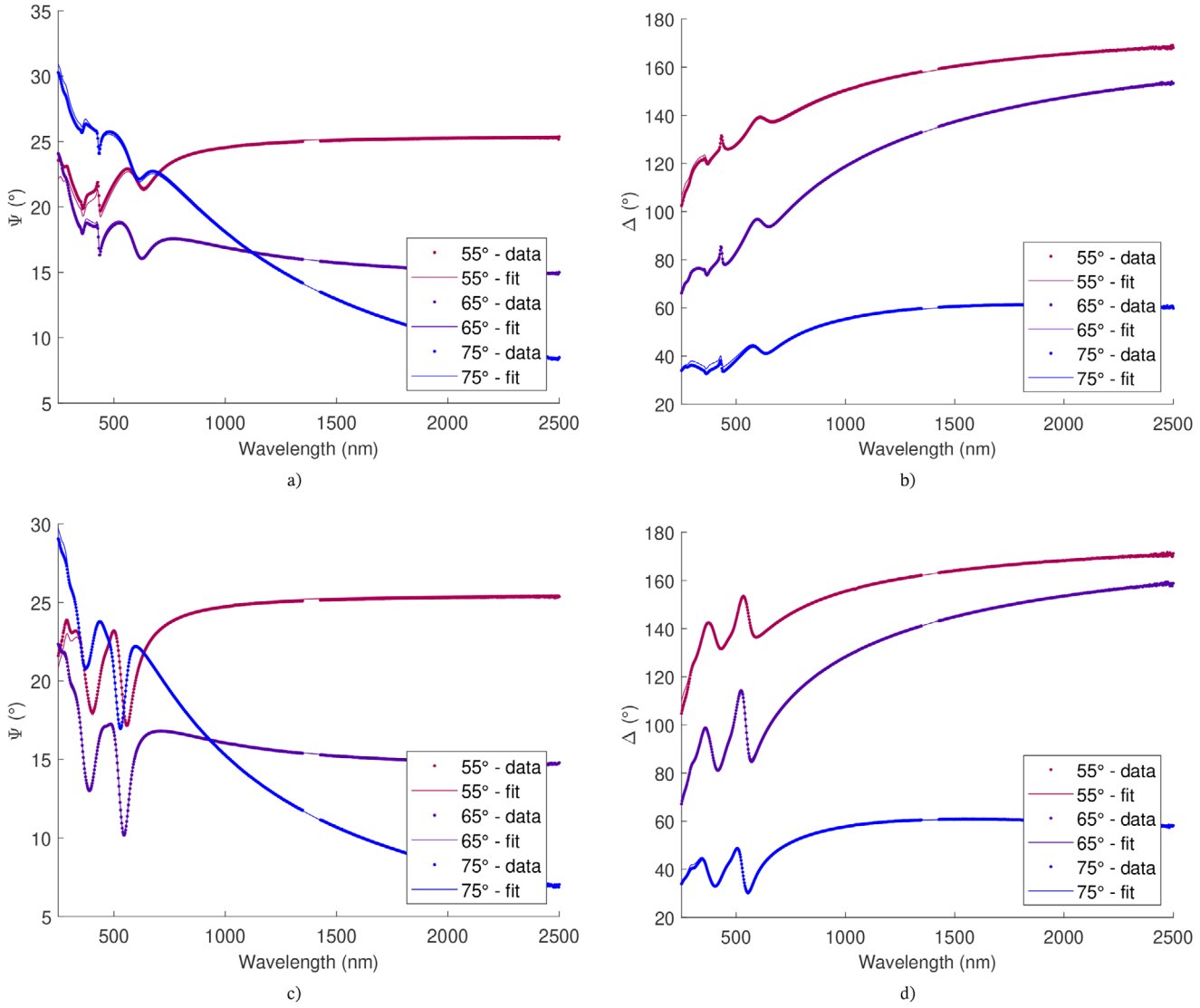

Figure 3. Representative ellipsometry fits for thin films. a,b) $CABI_{50nm}$ and c,d) CBI_{40nm}: measured Ψ and Δ (symbols) and model fits (solid lines) at three applied incidence angles.

In the case of CBI, our band-gap values from Elliott fit and Critical Point fit corresponded better to the excitonic peak (2.54 eV) reported for single crystal $Cs_3Bi_2I_9$ than the continuous absorption which was assigned for a much larger value (2.87 eV).[14] Our absorption onset matched better with the reference. The main difference between the absorption spectra for $Cs_3Bi_2I_6Br_3$ thin film here and $Cs_3Bi_2I_9$ single crystal in the literature was that we did not observe a distinct peak in the absorption spectrum. Instead, the absorption continuum began right after the exitonic part. The differences in absorption spectrum may arise, for example, from the halide mixing or the structural difference, that is, a thin polycrystalline film versus a bulk single crystal. A similar continuous absorption spectrum with a less distinct excitonic peak for mixed halide $Cs_3Bi_2I_6Br_3$ has been reported as well.[29] However, the absorption onsets for both $Cs_3Bi_2I_6Br_3$ and $Cs_3Bi_2I_9$ were reported for much lower values (below 2 eV) in that case.[29]

2.3. Optical Simulations

We utilized the obtained optical constants to run optical simulations of solar cells applying CABI and CBI, respectively, as an absorber (**Figures 5**; Figures S23 and S24, Supporting Information). Planar device structure was modeled with the following layers and thicknesses SiO_2 (2 mm)/FTO (400 nm)/c-TiO_2 (50 nm)/CABI or CBI (varying thicknesses)/Spiro-OMeTAD (50 nm)/Au (100 nm), see Figure 5a. Perpendicular irradiation of indoor and solar spectra were modeled. Given the wide band-gaps of CABI and CBI, the indoor application is more prominent, and simulations under solar spectrum were conducted for reference.

Based on the optical simulation, useful absorption (that is, the fraction of incident photons absorbed within the absorber above E_g) in CABI device oscillated between ca. 83 % and ca. 93 % at wavelengths from 400 nm to 626 nm, which corresponds to the band-gap (Figure 5b). Parasitic absorption was strong for short

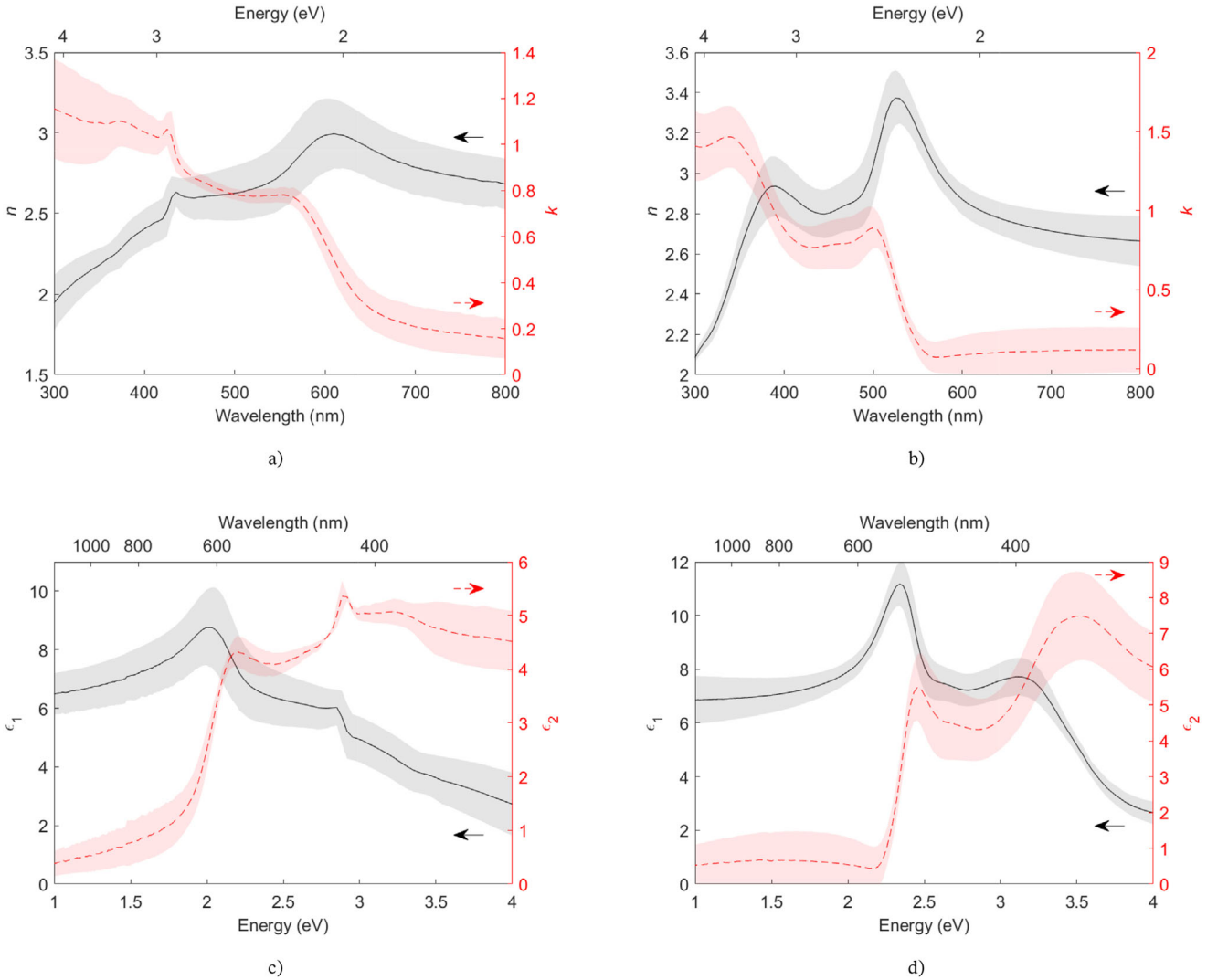

Figure 4. Optical constants of CABI and CBI. a,b) Refractive index and c,d) dielectric constant of CABI (panels a and c) and CBI (panels b and d). The shaded areas represent the standard deviations across different samples. For the full measurement range of 300–2500 nm, see Figure S11 (Supporting Information), and for the tabulated optical constant data, see Data Availability section.

wavelengths, but decreased toward 400 nm, and remained at or below ca. 5 % above 400 nm. Reflection oscillated between ca. 5 % and ca. 20 % over the studied wavelengths. The useful absorption sets an optical limit to the external quantum efficiency (EQE) which, thus, was simulated to vary around 85 % to 90 % over a broad wavelength range with the applied planar configuration and CABI layer thickness of 220 nm.

To estimate the maximum achievable photocurrent, the normalized absorption of CABI in the modeled solar cell was multiplied by an indoor irradiance spectrum, integrated until the bandgap wavelength, and converted to the units of electric current (Figure 5c). Perfect charge extraction was assumed to study the optical limit. The simulation predicted an integrated maximum achievable photocurrent (Int. J_{ph}) of 91.1 μA cm^{-2} (Figure 5c) under the modelled indoor irradiance with a color temperature of 4000 K and an illuminance of 1000 lx (500 lx: 45.5 μA cm^{-2}, 100 lx: 9.1 μA cm^{-2}, Figure 5d). Int. J_{ph} varied within 85–102 μA cm^{-2} under different color temperatures from 2700 to 6500 K with the constant illuminance of 1000 lx as shown in Figure 5d (see Figure S25, Supporting Information for the different indoor spectra, the data for 6500 K spectrum was previously published.[30]) Similar calculation under the modelled solar irradiance (AM1.5G; 1000 W m^{-2} power density) produced Int. J_{ph} of ca. 12.9 mA cm^{-2} (Figure S23, Supporting Information).

Table 1. Bandgap energies of the two Bi-PIMs obtained by different methods.

	Tauc plot (direct, allowed)	Elliott's model	Critical Point
CABI	1.98 eV	2.03 eV	2.09 eV
CBI	2.33 eV	2.43 eV	2.39 eV

Considering the uncertainty in the n and k spectra (Figures 4; Figures S13, Supporting Information), we performed sensitivity analysis for the optical simulation by linearly scaling the measured spectra with scaling factors (f_n and f_k) varying from 0.9 to 1.1 and from 0.5 to 1.5, respectively (Figure S26, Supporting Information). While one spectrum was varied, the other was kept constant. The two are related via Kramers-Kronig relations, but the purpose was to quantify the effect of the specific properties. Int. J_{ph} changed only little despite the large change in the absorption coefficient (Figure 5c). Int. J_{ph} decreased less than 4 % from ca. 91.1 μA cm^{-2} to ca. 87.7 μA cm^{-2} under indoor irradiance (3 W m^{-2}) and from ca. 12.9 mA cm^{-2} to 12.4 mA cm^{-2} under solar irradiance when f_k = 0.5. Interestingly, Int. J_{ph} decreased even in some cases with f_k > 1, which was due to stronger reflection (Figure S27, Supporting Information). However, the absorber layer thickness that was required for the maximal G_{ph} strongly depended on f_k (Figure S27, Supporting Information). The effect of the real part (n) was also small (Figure S23, Supporting Information), and the effect was more straightforward: higher n increased and lower n reduced the reflectance.

CBI device was modeled similarly to the CABI device (Figure S24, Supporting Information). Useful absorption varied between 85 % and 93 % in the wavelength range of 375 to 500 nm before decreasing towards the band-gap at ca. 530 nm. Reflection varied between 5 % and 16 % at wavelengths from 300 to 530 nm, and parasitic absorption decreased from 80 % at 300 nm to 5 % at 370 nm and remained at the level of 5 % or below until 530 nm (Figure S24, Supporting Information). Compared with the CABI cell, we obtained clearly smaller Int. J_{ph} for CBI cell: ca. 32 μA cm^{-2} under the indoor 4000 K and 1000 lx illuminance (500 lx: 16 μA cm^{-2}, 100 lx: 3.2 μA cm^{-2}, 21-50 μA cm^{-2} under different color temperatures from 2700 to 6500 K with the constant illuminance of 1000 lx) and ca. 7.2 mA cm^{-2} under the solar irradiance, respectively (Figure S24, Supporting Information). The wider E_g of CBI lead to the significant color temperature dependence of Int. J_{ph} due to the change in available photon flux with E_{photon} > E_g as illustrated also by the perfect absorption limit (Figure S24e, Supporting Information). As in the case of CABI device, we observed small changes in Int. J_{ph} when scaling the n and k spectra (Figure S24, Supporting Information). The optimal CBI layer thickness also changed with the f_k (Figure S28, Supporting Information).

The changes in the predicted photocurrent upon such large f_k variation were notably small. Despite slightly surprising at first, we find it fitting to the theory. According to Beer-Lambert law, light intensity attenuates exponentially when propagating in an absorbing medium. Therefore, most of the light is absorbed close to the front side anyway, and the order of magnitude is more important than the exact value. The exact value of the absorption coefficient tells the distance at which a given share of light is absorbed. Thus, the key parameter to consider was the absorber layer thickness (Figures S27 and S28, Supporting Information). We find the small change in Int. J_{ph} despite the varied absorption coefficient relate to the large enough absorber film thickness. The thinner the absorber layer, the stronger the dependence of the photogeneration on the absorption coefficient (Figures S29 and S30, Supporting Information). In addition, f_k strongly affected the CABI (or CBI) layer thickness to achieve a certain G_{ph} value (Figures S27 and S28, Supporting Information).

Radiative recombination limited operation was further calculated from the simulated photogeneration to demonstrate the more realistic optical limits of PCE (**Figure 6**) compared with the typical theoretical calculation with the perfect absorption above the band-gap, that is, the assumption of 100 % useful absorption up to the band-gap wavelength. At the radiative limit, Int. J_{ph} converted directly to short circuit current (J_{sc}), that is, ca. 91 μA cm^{-2} and ca. 13 mA cm^{-2} for the CABI device under indoor and solar irradiances, respectively (Figures 6a and 6b). The perfect absorption radiative limits of J_{sc} were ca. 106 μA cm^{-2} and ca. 15 mA cm^{-2} under indoor and solar irradiance, respectively, which were approximately 16 % higher than the radiative limits based on the simulated G_{ph} corresponding to the reflection and parasitic absorption losses (Figure 5b). CABI layer thickness affected J_{sc} and PCE as it affected G_{ph} (Figure 6b,c; Figure S29, Supporting Information). Minor effect on open circuit voltage (V_{oc}) was also observed (Figure S31, Supporting Information). Our calculation based on the simulated G_{ph}, produced the radiative-limited PCEs of ca. 42 % and 20 % under 4000 K WLED indoor and solar irradiance, respectively (Figure 6c). These limits increased to 49 % and 23 %, respectively, with the perfect absorption. The color temperature sensitivity of the PCE limits is presented in Figure S31 (Supporting Information). Corresponding radiative limits of PCE for CBI device were ca. 18 % and 13 % under indoor and solar irradiance, respectively, when the simulated G_{ph} was applied and ca. 21 % and 16 % under indoor and solar irradiance, respectively, assuming the perfect absorption (Figure S32, Supporting Information). The significantly lower PCE limits of CBI compared with CABI arise from its wider bandgap of ~2.4 eV.

Optical E_gs extracted from Tauc plots (direct, allowed transitions) were applied in the device simulations (Figures 5 and 6; Figures S24, and S32, Supporting Information). The bandgap values were a compromise considering both the electrical bandgap and the absorption onset. The electrical band gaps of CABI and CBI are likely somewhat larger than the applied values. However, we already left some absorption out of consideration for photocurrent when integrating photogeneration up to the band-gap wavelength instead of the actual onset (Figure 5b; Figure S24, Supporting Information). So, applying a larger or smaller bandgap would make one or the other issue more pronounced. Nevertheless, a self-consistent value was used with both materials, and sensitivity analysis on the effect of the bandgap value was also conducted providing quantitative estimations for the related uncertanties (Figures S33 and S34, Supporting Information).

The simulations showcased a high potential of especially CABI devices: the photocurrent generation of almost 100 μA cm^{-2} and the power conversion efficiency of ca. 42 % under indoor irradiance based on the measured optical properties (Figures 5 and 6). High limits were also obtained for CBI device but it was predicted to generate less current due to the larger bandgap. The calculated theoretical maximum efficiencies, that is, the radiative efficiency limits with perfect absorption, were 49 % for CABI and 21 % for CBI which agree well with the literature values for corresponding bandgaps.[1,31] The optical limit calculation with the actual device

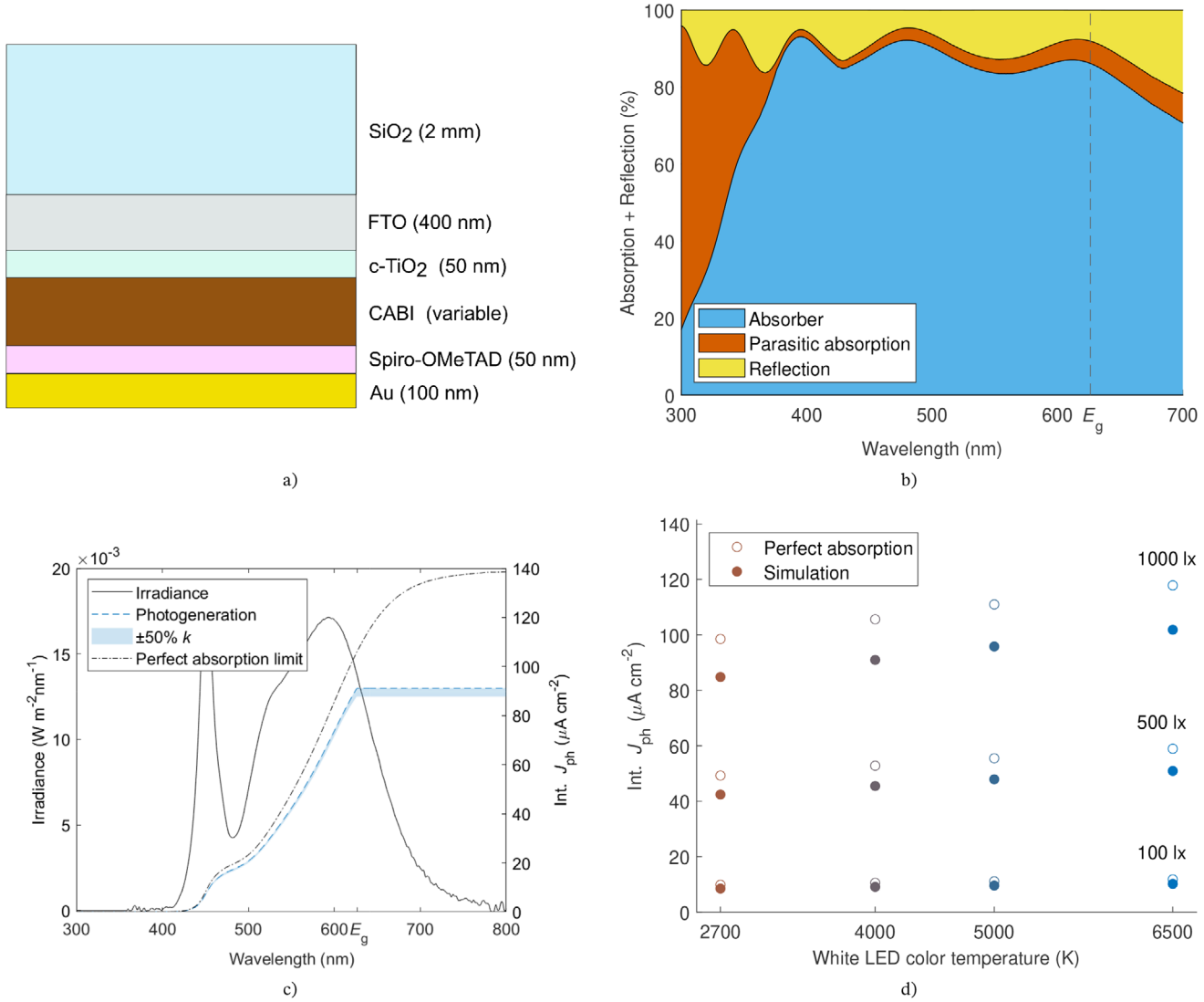

Figure 5. Optical response of a planar CABI photovoltaic cell. a) Illustration of the simulated planar device stack, figure is not to scale. b) Simulated reflection, absorption in CABI, and parasitic absorption in nonabsorber layers as a function of wavelength. CABI thickness of 220 nm (within the typical thickness range found in practical devices) was applied for this data. c) Simulated photocurrent generation (Int.J_{ph}) of the CABI device under indoor white light-emitting diode illumination (4000 K color temperature; 1000 lx illuminance/3 W m^{-2} spectral irradiance). Shown with *k*-scaling (0.5–1.5 ×) for sensitivity analysis. d) Int.J_{ph} under varying WLED color temperatures and illuminance levels.

structure and experimental optical constants provided more realistic theoretical limits. Imperfect absorption in the theoretical calculations has previously been modeled by 85 % external quantum efficiency and the reduction in the theoretical efficiency was very close to what we obtained.[31] However, the difference is that the limits presented here are more realistic albeit less general because the device structures and experimental material properties were strictly defined.

With the measured optics and the planar device stack, CABI achieved useful absorption of ≈85–90 % across most of the WLED relevant spectrum and a radiative limit PCE of ≈42 %, close to the indoor Shockley-Queisser envelope for $E_g \approx 2$ eV. Contemporary CABI IPV devices achieve ≈5–6 % at 1000 lx through strategies such as mesoporous TiO_2 thickness tuning and additive engineering, yet their performance remains limited by persistent self-trapping, non-radiative recombination, and transport/collection losses—highlighting the need for electrical modeling and defect/passivation approaches. At the same time, the produced optical constants could help to further improve the optics, especially from the device point of view. Our *k*-scaling shows that optical J_{sc} itself is insensitive to moderate α errors once absorbers are sufficiently thick, but optimal thickness and reflectance remain opportunities. Reflection was simulated to vary between 5 % and 20 % in the absorption range for both devices. Therefore, up to ca. 10 % relative improvement might be available by optical means. Reflectance could be minimized, for example, by anti-reflective coatings or light trapping structures. The optical constants, like the ones measured here, are needed for the design of such coatings.

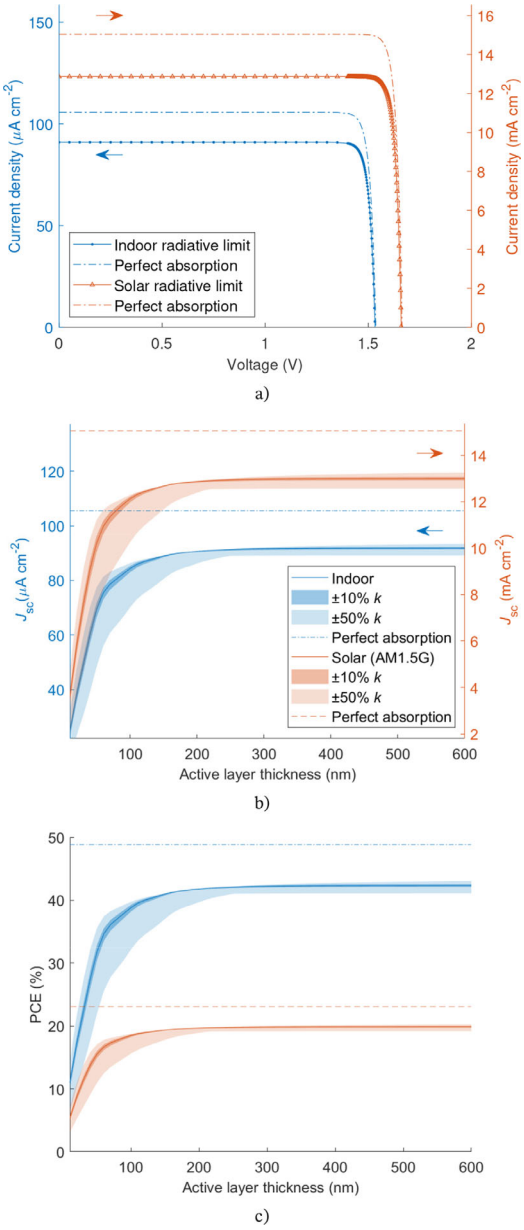

Figure 6. Radiative-limit performance of the CABI device with realistic optics. a) *J–V* curves at the radiative limit with CABI thickness optimized for 1000 lx 4000 K WLED indoor (220 nm) and AM1.5G (200 nm) lighting. b) Short-circuit current density, J_{sc}, versus CABI thickness for simulated G_{ph} and perfect absorption. c) PCE versus CABI thickness under the 4000 K WLED (1000 lx) and AM1.5G.

As a first try, 100 nm thick MgF_2 layer was added on top of the silica substrate of the CABI device (Figure S35, Supporting Information). G_{ph} improved by ca. 2 %. For further improvements, smoothening the difference of the refractive indices between the different layers at other interfaces should also be considered.

3. Conclusion

We report the optical constants of two thin film, lead-free Bi-PIMs (CABI and CBI), using spectroscopic ellipsometry, to enable accurate optical modeling of these promising IPV absorbers. Incorporating the measured optical data, we project a high optical limit for photocurrent generation (ca. 91 μA cm^{-2} J_{ph} at 1000 lx WLED illumination) for CABI under typical indoor lighting conditions (4000 K WLED; 3 W m^{-2} power density). The corresponding radiative-limit PCE for CABI in a realistic planar device stack (≈42 %) offers a more realistic theoretical efficiency ceiling compared to the idealized perfect absorption limit of almost 50 % often cited in the literature. There is a significant gap between the simulated optical limit for PCE (>40 %) and the current experimental state-of-the-art (≈5–6 %) achieved in CABI IPV devices, which suggests that electrical losses, rather than optical limitations, are the primary bottlenecks. The extracted optical constants and predicted photogeneration rates will enable detailed electrical device modeling, which is expected to deepen our understanding of current performance limitations and guide strategies to overcome them. These strategies may include defect passivation and optimization of charge transport, ultimately helping to close the efficiency gap in Bi-PIM IPVs.

4. Experimental Section

Materials: Silver iodide (AgI, 99.999 % metals basis) was acquired from Fisher. Bismuth(III) iodide (BiI_3, 99.998 % trace metals basis), bismuth(III) bromide ($BiBr_3$, 98 %), cesium iodide (CsI, 99.9 % trace metals basis), cesium bromide (CsBr, 99.999 % trace metals basis), copper iodide (CuI, 99.999 % trace metals basis), thiourea, dimethyl sulfoxide (DMSO, 99.9 % anhydrous), *N*,*N*-dimethylformamide (DMF, 99.8 %, anhydrous) and chlorobenzene (CB, anhydrous, 99.8 %) were purchased from Sigma–Aldrich. All chemicals were used as received without additional purification.

Fabrication of Bi-PIM Films: *Cu_2AgBiI_6 (CABI) Solution Preparation and Film Fabrication*:The CABI solution was prepared by mixing AgI (241.8 mg), CuI (238.1 mg), and BiI_3 (517.2 mg) into 1.5 mL of DMSO and 0.5 mL of DMF (3:1 DMSO:DMF ratio). The solution was stirred at 150 °C for 40 min, followed by overnight stirring at room temperature. The CABI solution (initial concentration defined as x) was further diluted to concentrations x/2 and x/3 by adding DMSO and DMF in the same 3:1 ratio. CABI films (with solution concentrations of x, x/2, or x/3) were prepared by spin-coating 100 μL of the solutions at 3000 rpm for 60 s. The solutions were heated to 75 °C prior to spin coating. Both solution preparation and spin coating were performed in a nitrogen environment. The films were then annealed in ambient air, first at 50 °C for 50 min and then at 200 °C for 4 min.

$Cs_3Bi_2I_6Br_3$ (CBI) Solution Preparation and Film Fabrication: The CBI solution was prepared by first preparing separate $Cs_3Bi_2I_9$ and $Cs_3Bi_2Br_9$ solutions. The $Cs_3Bi_2I_9$ solution was prepared by mixing CsI (175.4 mg), BiI_3 (265.3 mg), and thiourea (68.5 mg) into 0.8 mL of DMSO and 0.2 mL of DMF (4:1 DMSO:DMF ratio). The $Cs_3Bi_2Br_9$ solution was prepared by mixing CsBr (143.6 mg) and $BiBr_3$ into 0.8 mL of DMSO and 0.2 mL of DMF (4:1 DMSO:DMF ratio). Both solutions were stirred overnight at room temperature. The $Cs_3Bi_2I_9$ and $Cs_3Bi_2Br_9$ solutions were mixed in a 2:1 ratio to obtain the final CBI solution with the initial concentration x. This solution was further diluted to concentrations x/2 and x/3 by adding DMSO and DMF in the same 4:1 ratio. CBI films (with solution concentrations of x, x/2, or x/3) were prepared by spin-coating 100 μL of the solutions at 2000 rpm for 40 s. A volume of 170 μL of CBI antisolvent was added 5 s before the spin-coating program ended. The films were annealed at 135 °C for 30 minutes. All steps for CBI film preparation were performed in a nitrogen environment.

Characterization: The surface morphology of the samples was characterized by AFM (Park Systems NX10) and SEM (Thermo Scientific Apreo S Field-Emission Scanning Electron Microscope). The AFM images were processed using Gwyddion (version 2.68).[32] The AFM data was leveled by mean plane subtraction and the zero-height reference was determined from the height distribution onset. Energy-dispersive X-ray spectroscopy (EDS, Oxford Instruments Ultim Max 100 spectrometer) data was analyzed with AZtec (version 6.1.).

SE measurements were conducted with a J.A. Woollam VASE ellipsometer. Wavelength range of 300 –-2500 nm and incidence angles of 55 °, 65 °, and 75 ° were applied. Measurement analysis was performed using WVASE software. Graded Bruggeman EMA was applied to model the samples due to roughness.[18] Void volume fraction increased quasi-continuously through the sample layer. Twenty-one sublayers were used. Tauc-Lorentz oscillator model (with three oscillators) was applied for fitting the film thicknesses and void volume fraction distributions. The complex index of refraction was subsequently revised by point-by-point fit while keeping the film structure constant to find more accurate values for the optical constants and improve the fit.

Device Simulation: The net radiation method[33] based on the transfer matrix method[34–37] was applied to solve the wavelength specific local optical electric field in the simulated device under perpendicular irradiation. Local absorption, and subsequently the G_{ph} profiles as a function of depth in the active material were directly calculated from the local optical electric field.[36,37] Parasitic absorption in the respective electrode and transport layers and the reflection from the device were similarly calculated. Incoherent light propagation in the active material was assumed. Although the applied layer thicknesses are below the coherence length of sunlight (a coherent model could be applied), scattering at the absorber interfaces makes an incoherent treatment more realistic. Further details of the model implementation were given in our previous work.[38]

For the optical simulation, refractive index spectra are required as model inputs. The refractive index spectra of the active materials were measured here as described above. The spectra for the other layers, SiO_2,[39,40] FTO,[39,40] compact TiO_2,[39,40] Spiro-OMeTAD,[39,40] Au,[41] and MgF_2,[42,43] were taken from the literature.

Device operation at the radiative limit was calculated by subtracting the thermal emission from the photogeneration.[44] Current–voltage ($I - -V$) curves were calculated with the voltage dependent photon emission. Emitted photon current at a voltage V and temperature $T = 25$ °C was calculated by generalized Planck's law.[45,46] PCE, J_{sc} and V_{oc} were extracted from the $I - -V$ curves.

Supporting Information

Supporting Information is available from the Wiley Online Library or from the author.

Acknowledgements

The authors thank the LMD group at the University of Turku for helpful discussions about ellipsometry, Joaquin Valdez Garcia for helpful discussions about AFM, and Ermei Mäkilä for helpful discussions about SEM. A.K. thanks the University of Turku Graduate School (UTUGS), Jenny and Antti Wihuri Foundation and Lieto Savings Bank Foundation (KesPV project) for funding his doctoral research. M.H. thanks SUSMAT profiling funding (Research Council of Finland and University of Turku). G.K.G., S.T., and P.V. thank the SPOT-IT project founded by the CET Partnership, the Clean and Energy Transition Partnership under the 2022 CET Partnership joint call for research proposal, cofounded by the European Commission (GA 101069750) and with the founding of the organizations detailed on https://cetpartnership.eu/funding-agencies-and-call-modules. S.Y. and K.M. thank Circular Materials Bioeconomy Network funded by Ministry of Education and Culture, Finland (CIMANET, Decision No. VN/3137/2024-OKM-6). P.V. acknowledged funding from Research Council of Finland, Decision No. 347772. The work was part of the Research Council of Finland Flagship Programme, Photonics Research and Innovation (PREIN), Decision No. 346511. This study was conducted using MARI infrastructure at the University of Turku.

Author Contributions

A.K. conducted the characterization (ex. SEM) and simulations and wrote most parts of the initial draft. G.K.G. wrote parts of the initial draft. S.T. prepared the samples. S.Y. took the SEM images. A.K., G.K.G., M.H., P.V., and K.M. designed the study. P.V. and K.M. supervised the work. All authors participated in review and editing.

Conflict of Interest

The authors declare no conflicts of interest.

Data Availability Statement

The research data (https://doi.org/10.5281/zenodo.17899531) and the simulation scripts for the conducted computations (https://github.com/akamppinen/OpticsOfBiBasedPIMs) are publicly available.

Conflict of Interest

The authors declare no conflict of interest.

Keywords

indoor photovoltaics, lead-free perovskite-inspired materials, computational device simulation, spectroscopic ellipsometry, thin film

Received: October 1, 2025
Revised: December 1, 2025
Published online: January 9, 2026

[1] G. K. Grandhi, G. Koutsourakis, J. C. Blakesley, F. De Rossi, F. Brunetti, S. Öz, A. Sinicropi, M. L. Parisi, T. M. Brown, M. J. Carnie, R. L. Z. Hoye, P. Vivo, *Nat. Rev. Clean Technol.* **2025**, *1*, 132.
[2] I. Mathews, S. N. Kantareddy, T. Buonassisi, I. M. Peters, *Joule* **2019**, *3*, 1415.
[3] Y. Peng, T. N. Huq, J. Mei, L. Portilla, R. A. Jagt, L. G. Occhipinti, J. L. MacManus-Driscoll, R. L. Z. Hoye, V. Pecunia, *Adv. Energy Mater.* **2021**, *11*, 2002761.
[4] V. Pecunia, L. G. Occhipinti, R. L. Z. Hoye, *Adv. Energy Mater.* **2021**, *11*, 2100698.
[5] M. F. Müller, *Indoor Photovoltaics: Efficiencies, Measurements and Design*, chapter 8, 203–222, John Wiley & Sons, Ltd, ISBN 9781118845721, **2013**.
[6] Y. Cui, L. Hong, J. Hou, *ACS Appl. Mater. Interfaces* **2020**, *12*, 38815.
[7] M. Freitag, J. Teuscher, Y. Saygili, X. Zhang, F. Giordano, P. Liska, J. Hua, S. M. Zakeeruddin, J.-E. Moser, M. Grätzel, A. Hagfeldt, *Nat. Photonics* **2017**, *11*, 372.
[8] Q. Ma, Y. Wang, L. Liu, P. Yang, W. He, X. Zhang, J. Zheng, M. Ma, M. Wan, Y. Yang, C. Zhang, T. Mahmoudi, S. Wu, C. Liu, Y.-B. Hahn, Y. Mai, *Energy Environ. Sci.* **2024**, *17*, 1637.
[9] A. Babayigit, A. Ethirajan, M. Muller, B. Conings, *Nat. Mater.* **2016**, *15*, 247.

[10] F. Schmitz, R. Bhatia, F. Lamberti, S. Meloni, T. Gatti, *APL Energy* **2023**, *1*, 021502.
[11] S. T. Thornton, G. Abdelmageed, R. F. Kahwagi, G. I. Koleilat, *J. Chem. Technol. Biotechnol.* **2022**, *97*, 810.
[12] R. Wang, H. Li, H. Sun, in *Encyclopedia of Environmental Health (Second Edition)*, (Ed.: J. Nriagu), pp. 415–423. Elsevier, Oxford, second edition edition, **2019**, https://www.sciencedirect.com/science/article/pii/B9780124095489118706.
[13] G. K. Grandhi, S. Toikkonen, B. Al-Anesi, V. Pecunia, P. Vivo, *Sustainable Energy Fuels* **2023**, *7*, 66.
[14] S. Valastro, S. Gavranovic, I. Deretzis, M. Vala, E. Smecca, A. La Magna, A. Alberti, K. Castkova, G. Mannino, *Adv. Opt. Mater.* **2024**, *12*, 2302397.
[15] *Spectroscopic ellipsometry for photovoltaics*, (Eds.: H. Fujiwara, R. W. Collins) vol. *1*, Springer, Berlin **2018**.
[16] S. N. Savenkov, *Jones and Mueller matrices: structure, symmetry relations and information content*, Springer Berlin Heidelberg, Berlin, Heidelberg **2009**, pp. 71–119.
[17] H. Fujiwara, *Effect of Roughness on Ellipsometry Analysis*, Springer International Publishing, Cham **2018**, pp. 155–172.
[18] D. Lehmann, F. Seidel, D. R. Zahn, *SpringerPlus* **2014**, *3*, 82.
[19] H. C. Sansom, G. Longo, A. D. Wright, L. R. V. Buizza, S. Mahesh, B. Wenger, M. Zanella, M. Abdi-Jalebi, M. J. Pitcher, M. S. Dyer, T. D. Manning, R. H. Friend, L. M. Herz, H. J. Snaith, J. B. Claridge, M. J. Rosseinsky, *J. Am. Chem. Soc.* **2021**, *143*, 3983.
[20] B. W. J. Putland, M. Righetto, H. Jin, M. Fischer, A. J. Ramadan, K.-A. Zaininger, L. M. Herz, H. C. Sansom, H. J. Snaith, *Adv. Energy Mater.* **2024**, *14*, 2303313.
[21] V. Sugathan, M. Liu, A. Pecoraro, T. K. Das, T.-P. Ruoko, G. K. Grandhi, D. Manna, H. Ali-Löytty, K. Lahtonen, A. B. Mu noz-García, M. Pavone, P. Vivo, *ACS Appl. Mater. Interfaces* **2024**, *16*, 19026.
[22] H. Fujiwara, S. Fujimoto, M. Tamakoshi, M. Kato, H. Kadowaki, T. Miyadera, H. Tampo, M. Chikamatsu, H. Shibata, *Appl. Surf. Sci.* **2017**, *421*, 276.
[23] M. Shirayama, H. Kadowaki, T. Miyadera, T. Sugita, M. Tamakoshi, M. Kato, T. Fujiseki, D. Murata, S. Hara, T. N. Murakami, S. Fujimoto, M. Chikamatsu, H. Fujiwara, *Phys. Rev. Appl.* **2016**, *5*, 014012.
[24] B.-W. Park, B. Philippe, X. Zhang, H. Rensmo, G. Boschloo, E. M. J. Johansson, *Adv. Mater.* **2015**, *27*, 6806.
[25] C. Wu, Q. Zhang, Y. Liu, W. Luo, X. Guo, Z. Huang, H. Ting, W. Sun, X. Zhong, S. Wei, S. Wang, Z. Chen, L. Xiao, *Adv. Sci.* **2018**, *5*, 1700759.
[26] G. Longo, S. Mahesh, L. R. V. Buizza, A. D. Wright, A. J. Ramadan, M. Abdi-Jalebi, P. K. Nayak, L. M. Herz, H. J. Snaith, *ACS Energy Lett.* **2020**, *5*, 2200.
[27] G. K. Grandhi, B. Al-Anesi, H. Pasanen, H. Ali-Löytty, K. Lahtonen, S. Granroth, N. Christian, A. Matuhina, M. Liu, A. Berdin, V. Pecunia, P. Vivo, *Small* **2022**, *18*, 2203768.
[28] L. R. V. Buizza, A. D. Wright, G. Longo, H. C. Sansom, C. Q. Xia, M. J. Rosseinsky, M. B. Johnston, H. J. Snaith, L. M. Herz, *ACS Energy Lett.* **2021**, *6*, 1729.
[29] B.-B. Yu, M. Liao, J. Yang, W. Chen, Y. Zhu, X. Zhang, T. Duan, W. Yao, S.-H. Wei, Z. He, *J. Mater. Chem. A* **2019**, *7*, 8818.
[30] N. Lamminen, J. Lahtinen, M. Krishnaiah, J. Karlsson, M. Saju, G. K. Grandhi, P. Vivo, *ACS Energy Lett.* **2025**, *10*, 3415.
[31] G. Burwell, S. Zeiske, P. Caprioglio, O. J. Sandberg, A. M. Kay, M. D. Farrar, Y. R. Kim, H. J. Snaith, P. Meredith, A. Armin, *Solar RRL* **2024**, *8*, 2400180.
[32] D. Nečas, P. Klapetek, *Cent. Eur. J. Phys.* **2012**, *10*, 181.
[33] R. Santbergen, A. H. Smets, M. Zeman, *Opt. Express* **2013**, *21*, A262.
[34] M. Born, E. Wolf, *Principles of optics*, 4. edition, Pergamon, Oxford **1970**.
[35] C. C. Katsidis, D. I. Siapkas, *Appl. Opt.* **2002**, *41*, 3978.
[36] L. A. A. Pettersson, L. S. Roman, O. Inganäs, *J. Appl. Phys.* **1999**, *86*, 487.
[37] G. F. Burkhard, E. T. Hoke, M. D. McGehee, *Adv. Mater.* **2010**, *22*, 3293.
[38] A. Kamppinen, H. Palonen, K. Miettunen, *ACS Appl. Energy Mater.* **2024**, *7*, 4324.
[39] E. Raoult, Dataset.xlsx, **2022**, https://opticapublishing.figshare.com/articles/dataset/Dataset_xlsx/16738531.
[40] E. Raoult, R. Bodeux, S. Jutteau, S. Rives, A. Yaiche, A. Blaizot, D. Coutancier, J. Rousset, S. Collin, *Opt. Express* **2022**, *30*, 9604.
[41] R. L. Olmon, B. Slovick, T. W. Johnson, D. Shelton, S.-H. Oh, G. D. Boreman, M. B. Raschke, *Phys. Rev. B* **2012**, *86*, 235147.
[42] M. N. Polyanskiy, *Sci. Data* **2024**, *11*, 94.
[43] H. H. Li, *J. Phys. Chem. Ref. Data* **1980**, *9*, 161.
[44] W. Shockley, H. J. Queisser, *J. Appl. Phys.* **1961**, *32*, 510.
[45] T. Trupke, E. Daub, P. Würfel, *Sol. Energy Mater. Sol. Cells* **1998**, *53*, 103.
[46] T. Trupke, M. A. Green, P. Würfel, *J. Appl. Phys.* **2002**, *92*, 1668.